Intra-night flickering of RS Ophiuchi: II. Exponentially distributed quasi-period modes

Ts. B. Georgiev[1], R. K. Zamanov[1], S. Boeva[1], G. Latev[1], B. Spassov[1], J. Martí[2], G. Nikolov[1], S. Ibryamov[3], S. V. Tsvetkova[1], K. A. Stoyanov[1]
[1] Institute of Astronomy and National Astronomical Observatory, Bulgarian Academy of Sciences, 72 Tsarigradsko Chaussee Blvd., 1784 Sofia, Bulgaria
[2] Departamento de Física (EPSJ), Universidad de Jaén, Campus Las Lagunillas A3-420, 23071 Jaén, Spain
[3] University of Shumen, 115, Universitetska Str., 9700 Shumen, Bulgaria
tsgeorg@astro.bas.bg

(Submitted on 27.02.2019. Accepted on 06.06.2019)

Abstract. Linearized and flattened light curves (29 in B band and 29 in V band) of the recurent nova RS Oph, taken in 2008–2017 by 5 telescopes, are analyzed. The purposes are (i) characterizing of the flickering phenomenon by various ways and (ii) justification of the "resonance" distribution of the modes of the flickering quasi-periods, found in Paper I. The typical observing circumstances are: monitoring duration 60–150 min, number of CCD frames 50–200 and time step 0.5-1.5 min.

Part 1 presents photometric diagrams, standard and range deviations of the light curves in dependence on the average flux, as well as the distributions of the skewness and kurtosis of the histograms of the light curves. The intra-night flickering contains local disk obscures/shots and global disk instabilities. It seems both processes alternate their superiority. The average skewness, 0.12±0.30, gives weak privilege to the local shots. The average kurtosis, –0.17±0.62, gives some privilege to the global instabilities. In contrast to the random process with bell-shaped distribution of the deviations, deficit of small and large deviations is obvious in about 1/2 of the cases. Presence of light variations, close to oscillations, give some priority to the global disk instabilities.

In Part 2 every light curve is scanned digitally by a system of data windows with sizes Θ. Six fractal parameters are derived as average values for each Θ and regarded as functions on Θ in log-log coordinates. The average structure gradient, 0.48±0.16, also does not point out the prior process of the light variations. The mean value of the fractal dimension, 1.48 ± 0.06, too. The asymmetry function, introduced in this work, shows that the mean duration of the elementary shots is 3.6±0.8 min. It seems the relatively weak and short local shots dominate at time scales of a few minutes.

Part 3 presents 97 quasi-periods and their distributions. The quasi-periods are detected by the local minima of the structure functions as 58 primary, 20 secondary, 10 tertiary and 13 very short. All quasi-periods are confirmed by the local maxima of the relevant auto-correlation function. The distribution of the quasi-periods shows 6 modes, at 8, 13, 21, 30, 48 and 73 min. The modes of the quasi-period P follow exponential (or power) function on the number of the mode M with standard deviation of 4.7%. The power dependence is $P_M = 3.48 \times 1.55^M$. This function predicts modes also at 3.5, 5.3 and 115 min, which are not detected in this work. However, the characteristic duration of the elementary shot, 3.6±0.8 min, corresponds well to the predicted mode at 3.5 min. Because $1.55 \approx 3/2$, the modes of the quasi-periods like obey 3/2 resonance with unknown reason. The relative energy of the quasi-period (i.e. of the quasi-periodic structure, including the energy of its substructures) correlates with the logarithm of the quasi-period under a slope coefficients 0.02.

Generally, the flickering light curves are too complicated and various, without a possible classification (at least in the present work). Unique systematic is only the resonance-like sequence of the quasi-period modes.

Key words: stars: binaries: symbiotic – novae, cataclysmic variables – accretion, accretion discs – stars: individual: RS Oph

Introduction

RS Oph is a symbiotic recurrent nova that contains an M2 III mass donor (Shenavrin, Taranova & Nadzhip 2011) and a massive carbon-oxygen white dwarf (Mikolajewska & Shara 2017). The orbit of the system is circular (Fekel et al. 2000) with period 453.6±0.4 d (Brandi et al. 2009). RS Oph exhibits recurrent nova outbursts approximately every 20 years (Evans et al. 2008) with most recent nova outburst that occurred on 2006 February 12 (Narumi et al. 2006). Wynn (2008) proposed that both Roche lobe overflow and stellar wind capture are possible accretion scenarios in the case of RS Oph.

The flickering (brightness variability on time scales from minutes to hours) of RS Oph has been first detected by Walker (1977). The peak-to-peak amplitudes of these variations reach 0.3–0.5 mag. Kundra, Hric & Gális (2010) carried out wavelet analysis of two time series of RS Oph. They unveiled two different modes of flickering, with frequency 50–100 c/d (cycles of variations per day) and < 50 c/d. The respective quasi-periods are 30–15 min and > 30 min. The amplitudes of the flickering modes are estimated to be about 0.1 mag and about 0.6 mag, respectively.

Later, Kundra & Hric (2014) revealed two flickering modes with frequency 60 c/d and 140 c/d, i.e. with quasi-periods 24 min and 10 min. The amplitudes are 0.6 mag and 0.1 mag, respectively. The flickering phenomenon is explained (roughly yet) by variable mass transfer from the red giant through the accretion disk to the surface of the white dwarf. The reasons of the appearance of two modes of flickering are not clear.

Recently, Zamanov et al. (2018) estimated the average values and amplitudes of the magnitude, color, temperature and radius of the flickering source. They found that while RS Oph becomes more blue as it becomes more bright, but the blue component becomes more red as it becomes more bright (assuming that the red component is not variable). Zamanov et al. (2018) found also a correlation with coefficient 0.81 between the B band magnitude and the radius of the flickering source. They did not find correlation between the temperature and the brightness of the flickering source.

More information, especially about the influence of the brightness state on the observing particularities of the flickering is necessary. The flickering parameters vary from night to night and the study of the physics of the flickering requires revealing of time details of the variability. Such details ought to be characterized by their typical time scales, amplitudes, standard deviations, morphologies, etc. The data about the flickering source are of main interest.

Information from the apparent chaos of the flickering may be extracted in different ways, as well as by a system of statistical methods, considered today as fractal analysis. The fractal approach is preferable because (i) being conceptually simple, it extracts from the apparent chaos numerous useful parameters, (ii) it is weakly sensitive to non-equality of the data sampling and (iii) in contrast to the Fourier techniques it is applicable at low signal-to-noise ratio.

Similar approach has been applied by Bachev et al. (2011) and Georgiev et al. (2012) for studying of the flickering of the cataclysmic variable star

KR Aur. The main result is that the flickering contains at least two different sources of variability.

In Paper I (Georgiev et al. 2019) we explored magnitude scales. We found quasi-periodic structures with sizes 10–120 min in all flickering series. We unveiled four modes of quasi-periods, at about 10, 21, 36 and 74 min. The quasi-period of about 21 min is the most widespread. Also, we found a faint correlation between the quasi-period and its cumulative flickering energy, estimated by the plateau level of the relevant deviation function.

In the present paper we explore linear flux scales. We concentrate (i) on revealing parameters and functions for quantitative characterizing of flickering light curves (Fig. 5) and (ii) on re-revealing the modes of the quasi-periods with sizes 15–80 min by more exact criteria (Fig. 12). The light fluctuations of the RS Oph are too various and therefore we compare them with the known fluctuations of the sunspot index of Wolf for 6 cycles and the number of the visits in the Smolyan planetarium for 6 years (Fig. 7), as well as with uniform and normal random processes.

Numerical results of the processing are presented in 5 tables, in Appendix A. Fifty-eight panels with graphs, similar to these in Fig. 5, are collected in Appendix B as Supplement Gallery, cited hereafter "Gallery". Appendix B is available only in the electronic version of Bulgarian Astronomical Journal.

Contents of the text follows:

In this paper some abbreviations are used, as follows:
AF - asymmetry (ratio) function (Sect. 2.5);
A′F - skewness (asymmetry) function (Sect. 2.5);
BT - breakdown time-point (Sect. 2.5);

CC - correlation coefficient;
DF - (standard) deviation function (Sect. 2.2);
FS - flickering source (Introduction);
FD - fractal dimension (Sect. 2.4);
HF - Hurst function (rescaled range function, Sect. 2.4);
HG - Hurst gradient (Sect. 2.4);
MLC - Monitoring light curve (Introduction);
RD - range deviation (half of the peak-to-peak amplitude, Sect. 1.3);
RF - range (deviation) function (Sect. 2.3);
SD - standard deviation of histogram or regression;
SE - standard error of estimated value;
SF - structure (deviation) function (Sect. 2.3);
SG - structure gradient (Sect. 2.3);
QP - quasi-period (Sect. 2.3, 3.1).

1. General view on the monitoring light curves (MLCs)

We analyzed 29 pairs of quasi-simultaneous MLCs of RS Oph system, in B and V bands. These are the observations analyzed in Zamanov et al. (2018) to which MLCs #29B and #29V (20090614) are added. The observations were carried out by CCDs with the 2 m RCC, the 60 cm Cassegrain and the 50/70 cm Schmidt telescopes of the Rozhen NAO, the 60 cm Cassegrain telescope of the Belogradchik AO, as well as the 41 cm telescope of the University of Jaén, Spain, in 2008–2017. The observing material is presented in Zamanov et al. (2018; Table 1) and Georgiev et al. (2018; Paper I; Table 1), as well as in Table 1 and Table 2 in the present paper. The results are collected here in Tables. 3, 4 and 5.

The duration of a single monitoring run is $T_{\rm M}$ = 28–223 min, typically 60–150 min. The number of the data points n (CCD frames in a single run) 32–470, typically 50–200. The time steps of the MLC, $\tau_{\rm M} = T_{\rm M}/N_{\rm M}$, are 0.24–3.48 min, typically 0.5–1.5 min. The standard error of our photometry is 0.005–0.010 mag.

1.1. Photometric diagrams of the flickering source

In this work, magnitude data about the flickering source (FS) are derived after removal of the contribution of the red giant and account of the interstellar reddening. According to Zamanov et al. (2018) the apparent magnitudes of the red giant, considered to be constants, are $m_B = 14.66$ mag and $m_V = 12.26$ mag, with standard errors (SEs) 0.05 mag. The color excess toward RS Oph is estimated to be $E(B-V) = 0.69$ with SE 0.09 mag. The magnitude corrections $A(B) = 4.19 \times E(B-V)$ and $A(V) = 3.16 \times E(B-V)$ are applied.

The average magnitude and color index of each original MLC are given in Paper I. The average magnitudes of MLCs of the FS (after "removal" of the red giant and de-reddening) are given in Tables 3 and 4. The general average magnitudes and colors of all 29 pairs of MLCs are: $B = 9.36 \pm 0.40$

mag (from 8.58 to 10.15 mag), $V = 9.35 \pm 0.53$ mag (from 8.39 to 10.36 mag) and $(B - V) = 0.01 \pm 0.17$ mag (from –0.35 to 0.29 mag).

The first preliminary task is the visualization of the main photometric particularities of the FS. Zamanov et al. (2018, Fig. 4, Fig. 5) already show color-magnitude diagrams (CMDs), observed and calculated for the FS, based on B magnitude. Here we add the time behavior of the magnitude and color, as well as CMD, based on V magnitude.

Figure 1(a,b) presents the photometric behavior of the FS in the observing period. The V magnitude and $(B - V)$ color vary in the frames of ≈ 2 mag and ≈ 0.5 mag, respectively. Well pronounced minimum of the brightness and color is seen in the middle of the observing period, in 2013–2014. In agreement with Zamanov et al. (2018), when the average brightness is lower, then the average color is more blue. This circumstance is clearly revealed here in Fig. 1(c).

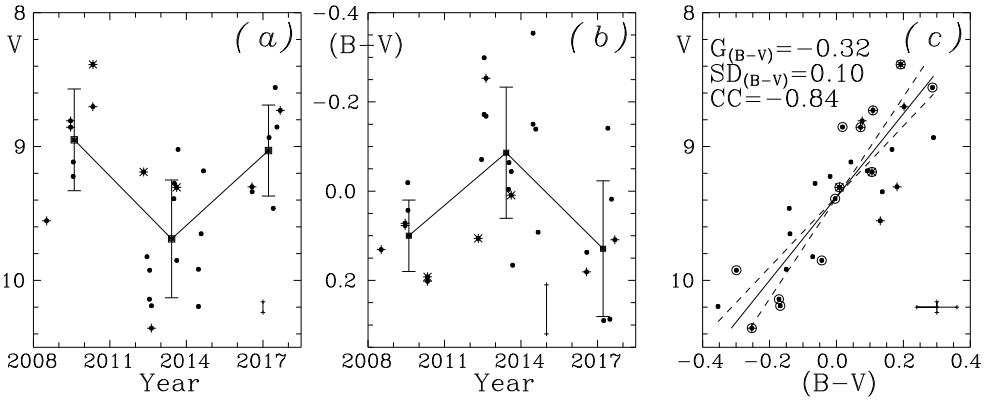

Fig. 1. (a,b): Behavior of the average V magnitude and $(B - V)$ color of the FS (dots) in 2008–2017. **(c):** CMD of the FS with ordinary and reverse regressions (dashed lines) plus their bisektrise (solid line). The MLCs which contain 2 or 3 quasi-periods (Sect. 3.2) are marked by crosses or asterisks, respectively. Typical individual error bars are shown in the right bottom corners of the diagrams. Hereafter "G", "SD" and "CC" are the gradient, standard deviation of regression and correlation coefficient, respectively .

Figure 1(c) presents CMD of the average magnitude V and average color $(B - V)$ of the MLC for the FS. The ordinary and reverse regressions are drown to visualize how much the dependence between both magnitudes and colors is narrow. The color gradient (here – the slope coefficient of the bisektrise between the ordinary and reverse regression) is $G(B - V) = \Delta(B - V)/\Delta V = -0.32$. The respective standard deviation (SD) is 0.10 and the correlation coefficient (CC) is –0.84. These parameters for the CMD with B instead V are –0.44, 0.14 and –0.69, i.e. the CMD based on V magnitudes is clearly narrower. We note also the remarkable close cor-

relation between V and B magnitudes with $CC = 0.87$, $G(B) = 0.76$ and $SD(B) = 0.02$.

In Fig. 1 the crosses mark MLCs in which 2 different quasi-periods are revealed (10 in B and 10 in V band). The asterisks mark the MLCs with 3 different quasi-periods (3 in B and 3 in V band, Sect. 3.2). More then one quasi-period seems to be present somewhat in more bright and more red MLCs.

1.2. Linearized, flatten and relative MLCs

The original MLCs of the FS, derived in B and V magnitude after removal of the red giant and de-reddening (Sect. 1.1), are linearized (transformed from magnitude scale to linear scale of flux) by the constants of Bessel (1979). For a zero-magnitude star these constants are 6.317×10^{-9} erg cm^{-2} s^{-1} Å^{-1} for B band and 3.619×10^{-9} erg cm^{-2} s^{-1} Å^{-1} for V band. In this work the results are expressed in units of 10^{-14} erg cm^{-2} s^{-1} Å^{-1}. The **linearized MLCs** $F(t)$ ($b(t)$ or $v(t)$) are shown in Figs. 5(a), 6(a) and top panels in the Gallery.

Linearizing only is not sufficient. The empiric functions for characterizing the MLC (Part 2) require flat MLCs, i.e. MLCs that fluctuate about a global constant. However, most of the original MLCs are significantly biased or they look like parts of flux variations with time scales of a few hours. The flattening of the linearized MLCs is unavoidable. In Paper I linear flattening (unbiasing) of the MLCs is applied in magnitude scales. The substantiate is the magnitude variations are small. In this paper, in the linear scale, the contrast of the MLC variations is increased and polynomial removal of the large scale trend is necessary.

For the flattening the linearized (in fluxes) MLC $F(t)$ is fitted by a polynomial of m-th degree, $f^{(m)}(t)$, and the polynomial is extracted from the MLC: $\Delta F(t) = F(t) - f^{(m)}(t)$. Then the **flattened residual MLC** $\Delta b(t)$ or $\Delta v(t)$ is:

$$\Delta b(t) = b(t) - f_{\rm b}^{(m)}(t) \quad \text{or} \quad \Delta v(t) = v(t) - f_{\rm v}^{(m)}(t). \tag{1}$$

In comparison with the linearized MLCs, the range and the standard deviation of the flattened residual MLC are decreased by average of 1.7 ± 0.8 times (up to 5.7 times). The flattened MLCs are not shown especially, but they are used in the dependences between the average flux and the standard deviation, or range deviation, of the MLC in Fig. 2(a,b).

We explore mainly MLCs which consist of relative deviations from the polynomial fit, $\delta F(t) = \Delta F(t)/f^{(m)}(t)$, expressed in percents, i.e. **relative residual MLC** $\delta b(t)$ or $\delta v(t)$:

$$\delta b(t) = \Delta b(t)/f_{\rm b}^{(m)}(t) \quad \text{or} \quad \delta v(t) = \Delta v(t)/f_{\rm v}^{(m)}(t). \tag{2}$$

These relative MLCs are shown in Figs. 5(b), 6(b) and in the Gallery, just below the top panels. The relative MLCs are easily compatible – directly and by their histograms (Figs. 5(c), 6(c), Gallery).

Suitable (low) polynomial degree is chosen for every MLC. The aims are: (i) describing the large scale trend of the MLC and (ii) agreement between the quasi-period estimations from the structure function and autocorrelation function (Sect. 3.2). The polynomial degrees and the numbers of their applications in this work are presented by the next pairs of numbers: 0-1, 1-4, 2-4, 3-35, 4-2, 5-9, 7-3. Example of the influence of the polynomial degrees 1, 3, 5 or 7 on the results in this study are given in Fig. 6. Generally, the results depend somewhat on the applied polynomial degree. However, such suppressing or removing of long time flux variations offsets the structures with time sizes 15–80 min and especially below 60 min.

We ought to note also that a small difference between the magnitudes Δm and the relative flux difference of the type $\delta F = \Delta F/F$ obey the Pogson's formulas[4] (Zombeck 1990):

$$\Delta m = 2.5 \times \lg(\delta F + 1) \qquad \text{or} \qquad \delta F = \mathrm{dex}(0.4 \times \Delta m) - 1. \qquad (3)$$

for $\Delta m \geq 0$ and $\delta F \geq 0$. Then the number of the hundreds of the magnitude difference (cmag) coincide well with the numbers of the percents of the relative flux difference, in percents in the interval 1–25 cmag or 1–25 percents.

Further, putting 1 in Eqs. 3 instead 2.5 and 1 instead 0.4 we derive the known formulas for transforming of relative difference in linear scale δF into difference in logarithmic scale $\Delta \lg F$ or vice versa: $\Delta \lg F = \lg(\delta F + 1)$ or $\delta F = \mathrm{dex}(\Delta \lg F) - 1$. Other such formulas, used in this paper (Figs. 11 and 12), are $\Delta \ln F = (\delta F + 1)$ and $\delta F = \exp(\Delta \ln F) - 1$.

1.3. Relations "average flux – flux deviation" of the flatten MLCs

The standard deviation (SD) and the range deviation (RD, the half of the peak-to-peak amplitude) of the flattened MLC are "energetic" characteristics of the flickering. They are directly available from the flattened residual MLC (Eqs. 1). These parameters correlate with the flux state of RS Oph (Zamanov et al. 2015, 2018). Therefore, the second preliminary task ought to be a revisiting of these correlations for the FS in magnitude and linear scales.

Figure 2(a) juxtaposes in magnitude scales the average magnitudes and the RD or SD of the MLCs. The RD and SD data take larger areas in V band. The ΔV data anti-correlate weakly with the average magnitudes, with $CC = -0.34$ for RD and $CC = -0.45$ for SD. The respective V gradients are $G_{\mathrm{RD}} = 0.013 \pm 0.027$ and $G_{\mathrm{SD}} = 0.025 \pm 0.070$. Both V gradients overcome the 95% Student's criterion of significance, while B gradients are practically zero.

So, at least in V band, the energy of the flickering is relatively larger in low state of the FS. Such conclusions about the flickering of the cataclysmic binary KR Aur in all bands has been pointed out by Bachev (2011) and

[4] In accordance with the International Organization for Standardization (ISO31-11) the notation lgX instead $\log_{10}$X or logX is fully admissible. (Taylor, B.N., 1995, Guide for the Use of the International System of Units (SI), US Department of Commerce.

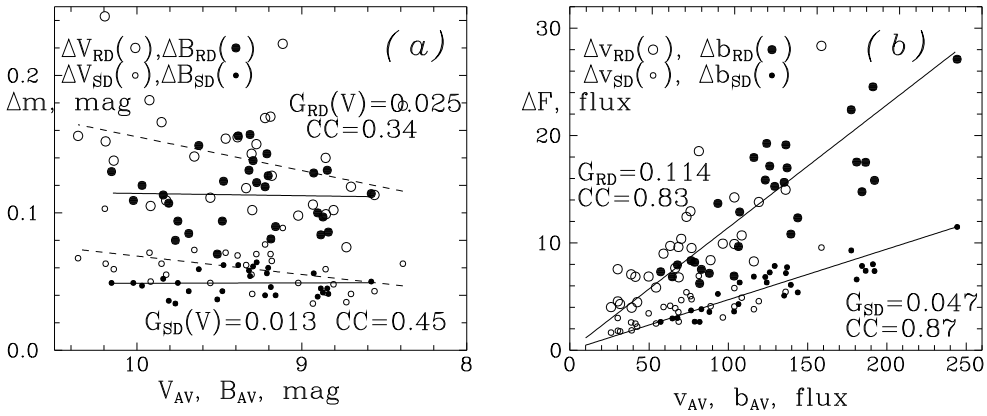

Fig. 2. Correlations between the range deviation (top) and the standard deviations (bottom) with the the average value of the MLC. (**a**): in magnitude scale; (**b**): in linear scale. Dots and circles present B and V data, respectively. The lines are the ordinary regressions; In (**b**) – together for B and V data, regressions without intercepts.

Georgiev et al. (2012). However, the difference between the high and low states for KR Aur is about 6 mag, while here it is 2 mag.

Figure 2(b) shows in the linear scale the approximate proportionality of the RD and SD to the MLC average, both for B and V data. The gradients are $G_{\rm RD} = 0.114 \pm 0.031$ and $G_{\rm SD} = 0.047 \pm 0.020$ with respective correlation coefficients 0.83 and 0.86. The ratio $G_{\rm RD}/G_{\rm SD} = 2.4$ is somewhat small and corresponds to the visual impression about some deficiency of strong deviations in the MLCs. In a simulated normal random process this ratio increases to 3 with the number of the simulated data is barely 100.

Figures 2(a) give evidences that the typical relative energy of the flickering in B band is 5% for SD and 11% for RD. In V band, in the frames of 2 mag increasing of the abscissa, the energy of the flickering decreases from 8% to 5% for SD and from 18% to 11% for RD. For comparison, the fluctuations of the sunspot index and the planetarium visits are essentially higher – about 90% and 75% for SD, respectively and about 200% for RD (Fig. 7(d)).

1.4. Histogram parameters of the relative MLCs

The third preliminary task ought to be general characterizing of the relative MLCs (Eqs. 2) by means of their histograms, shown in sub-figure (c) in Figs. 5–7, and in the Gallery. The histograms reflect a big variety of the MLC shapes.

The shape of any finite distribution $F_i, i = 1, 2, ..., n$ may be characterized by its standard deviation, SD, skewness (asymmetry) A' and kurtosis (excess) E'. The relevant formulas are based on the 2-nd, 3-rd and 4-th central moments of the distribution, m_2, m_3 and m_4, respec-

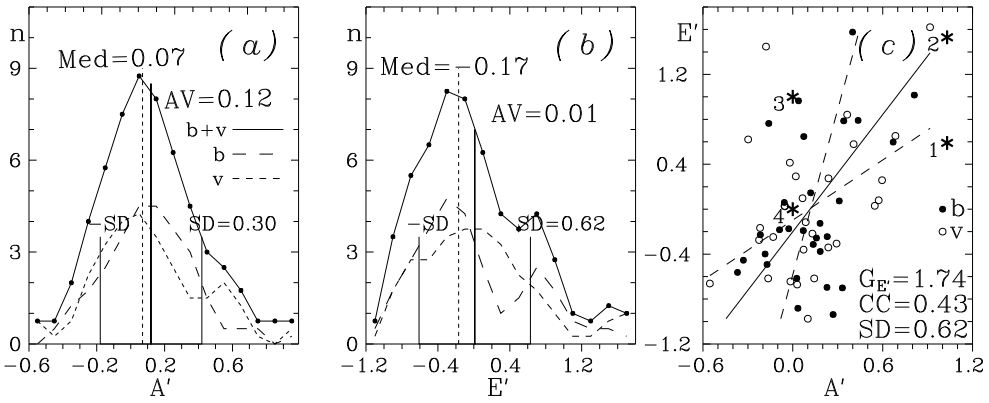

Fig. 3. (**a,b**): Distributions of the skewness A' (Eqs. 5) and the kurtosis E' (Eqs. 6) of the histograms of 58 relative MLCs (Eqs. 2). Dashed and short-dashed curves correspond to B and V MLCs, while the solid curves show the common distributions. (All histograms in this paper are slightly smoothed by convolution kernel [0.25, 0.50, 0.25]; (**c**): Juxtaposition of A' and E'. Dashed lines present the ordinary and reverce regressions while the solid line is their bisektrise.The asterisks show the data about the sunspot index (1) (Fig. 7, left panes), visits in the Smolyan planetarium (2) (Fig. 7, right panels), uniform random process (3) and normal random process (4).

tively. By definition $m_k = [\Sigma(F_i - F_{\rm m})]^k/n$, where $F_{\rm m}$ is the average value, $F_{\rm m} = [\Sigma F_i]/n =< F_i >$ and n is the number of data points.

The definition of the standard deviation for large sample of data and the formula for application on not large sample of data are:

$$SD(def) = m_2^{1/2} \quad \text{and} \quad SD = [m_2 \times n/(n-1)]^{1/2}. \tag{4}$$

The standard deviation s is regarded in dependence on MLC average in Sect. 1.3.

The definition of the skewness and the formula for sample application are:

$$A'(def) = m_3/m_2^{3/2} \quad \text{and} \quad A' = [n(n-1)]^{1/2}/(n-2) \times A'(def). \tag{5}$$

The definition of the kurtosis and the formula for sample application are:

$$E'(def) = m_4/m_2^2 - 3 \quad \text{and} \quad E' = Q_1 \times E'(def) - 3 \times Q_2. \tag{6}$$

Here $Q_1 = n^2(n+1)/[(n-1)(n-2)(n-3)]$ and $Q_2 = (n-1)^2/[(n-2)(n-3)]$). The formulas for sample applications are derived by Joanes & Gill (1998).

The normal random distribution is characterized by $A' = 0$ and $E' = 0$. Positive skewness, $A' > 0$, corresponds to distribution with heavy right wind (tail) and vice versa. Positive kurtosis, $E' > 0$, corresponds to distribution whose peak is more sharp than the peak of the normal distribution and vise versa. The uniform random distribution with scatter interval 1 has $A' = 0$ and $E' = 1$.

In Fig. 3(a) the skewness A' of the MLC (Eqs. 2) shows unimodal distribution, from –0.6 to 0.8, with peak about $A' = 0.1$. This distribution confirms again the visual impression that MLCs with large single deviations are very rare. Only one strong shot is clearly visible in MLC #17V. The slightly positive mode gives weak privilege of the positive deviations due to local disk shots. For comparison, the sunspot index and the planetarium visits, dominated obviously by positive shots, demonstrate high positive skewness (Fig. 7(c)). In the MLCs, in time scales < 15 min the steep flux changes are well visible in the MLCs. They are detected objectively by the suitable asymmetry indicator, introduced in this work (Sect. 2.5).

In Fig. 3(b) the kurtosis E' of the MLCs (Eqs. 2) is distributed more widely, from –1.2 to 1.4, with a peak about –0.2. Some right B appendage is seen in B band. The negative mode of E' confirms the visual impression that numerous histograms (about 1/2 of all) pose flat tops, like a histogram of a uniform random process. The reason is deficiency of small (close to the mean) flux variations. Then the fluctuations seem rather oscillations than normally distributed deviations.

A deficit of small flux variations is clearly visible when the polynomial fit passes well in the middle of the deviations of the linearized MLC, as in Fig. 5, top panels. Otherwise, about 1/4 of the histograms possess peaked tops (positive kurtosis) and significant skewness (positive or negative). The reason is that a part of the polynomial does not pass in the middle of the deviations and by this way it changes artificially the distribution of the deviations (Fig. 6(c), case $m = 3$). Figures 6(c) show how much the histogram shape changes when the polynomial degrees increase, tending in this case to histogram with positive kurtosis.

Generally, the negative mode of the distribution of the kurtosis (Fig. 3(b) gives evidence of certain preferences of the flux oscillations to the flux deviations, i.e. of some domination of the global disk instabilities over the local disk shots. However, it seems that both processes alternate their superiority.

Figure 3(c) shows the mutual distribution of the skewness A' and the kurtosis E'. The correlation coefficient, $CC = 0.43$, is low and the gradient of the bisektrise regression, $G = 1.74$, is poorly defined. In our opinion this correlation is due occasionally to the cases when the polynomial fit does not pass well in the middle of the linearized MLC. For a comparison, note that the histograms of the sunspots index and the planetarium visits ("1" and "2" in the diagram), pose clear positive skewness and kurtosis (Fig.7(c)).

So, in spite of the lack of clear systematics and dependences about the flux variations in the MLCs, two particularities of these variations could be noted, in contrast to the distributions of the normal randoms, sunspot index and planetarium visits: (i) a general deficiency of single large positive and negative deviations and (ii) a particular deficiency of small deviations. By these particularities some histograms of MLCs look like histograms of oscillations, similar to a uniform random process. Usually such histogram has flat or trident top with size about 2×SD (Figs. 5(c), 6(c), Gallery).

2. Fractal view on the MLCs

The aim of the data processing in this work is revealing and characterizing of specific particularities of the apparent chaos in the MLC. Special attention is devoted to the repeating time structures and their quasi-periods (QPs). Following the recommendations of Mandelbrot (1982), Russ (1994), Hastings & Sugihara (1995) and Falkoner (1997) we explore empiric fractal indicators, parameters and functions. The current results are shown in the relevant diagrams, collected in Figs. 5–7 and in the Gallery. Note that in Fig. 5 the MLCs in B and V band are obviously different because they are taken consecutively by one telescope.

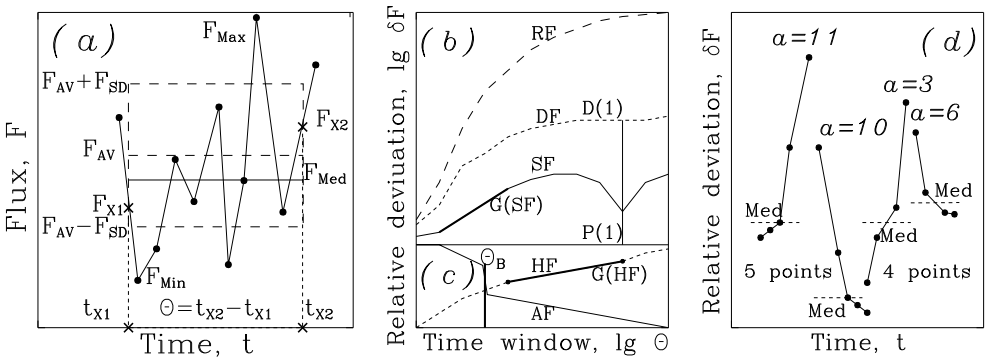

Fig. 4. (**a**): The window with size Θ_j on its k-th position in the MLC (dots, connected with segments), within the time bounds t_{X1} and t_{X2}. The respective 4 fractal indicators are are described in the text. (**b,c**): Typical shapes of 5 fractal functions over lg Θ, described in Sect. 2.2–2.5: Range function (RF, dashed curve) in (b), density function (DF, short-dashed curve) in (b), structure function (SF, solid curve) in (b), Hurst function (HF, short dashed curve, in (c)) and asymmetry function (AF, solid curve, in (c)). The gradients of the quasi-linear parts of the SF and HF, SG and HG, are noted as G(SF) and G(HF). P(1) is the quasi-period corresponding to the local minimum of the SF. D(1) is the density level of the DF, corresponding to P(1). Θ_B is the time breakpoint of the AF. (**d**): Often happening configurations of 5 or 4 adjacent points in the minute time scale, whose relative fluxes cause high values of the AF (Sec. 2.5), giving evidence that the MLC contains elementary shots.

2.1. Fractal indicators, parameters and functions

This study of a discrete MLC $F(t_n), n = 1, 2, , N$, is based on a system of scanning data windows with time sizes $\Theta_j, j = 1, 2, , J$. The window sizes are distributed uniformly by lg Θ. Each j-th window scans the MLC (with 1/2 overlapping), taking $k = 1, 2, , K$ different positions. The k-th position of the j-th window is shown in Fig. 4(a).

Every window position is used for calculation of fractal indicators. Every indicator is averaged over all K positions of the j-th window to give relevant

fractal parameter. The dependence of every parameter on the window size in log-log coordinates is considered as fractal function (Sect. 2.2–2.5).

The number of the specified window sizes is adopted to be J=99. In the scanning every wide window is used if it is applied on the MLC at least 3 times, and every narrow window is used if it contains at least 3 adjacent MLC points. Thus, we derive fractal functions with high resolution in which every point is based on many windows positions, from 3 to ≈120. The processing is organized in a few C-codes.

Figure 4(a) illustrates the definitions of 4 **local fractal indicators**: (standard) deviation indicator d_{jk}, structure indicator s_{jk}, range indicator r_{jk}, and asymmetry indicator a_{jk}. Further, the average value of every indicator over all K positions of the j-th window is derived as **global fractal parameter**: deviation parameter D_j, structure parameter S_j, range parameter R_j and asymmetry parameter A_j.

The deviation indicator d_{jk} and the deviation parameter D_j are:

$$d_{jk} = F_{\rm SD}, \qquad \text{and} \qquad D_j =< d_{jk} >_j \ . \tag{7}$$

Here $F_{\rm SD}$ is the standard deviation of the data in the current position of the window. And the broken brackets express average over all K positions of the j-th window. In Fig. 4(a) the average value $F_{\rm AV}$ and the rectangle, bounded by the levels $F_{\rm AV} \pm F_{\rm SD}$ in the window, are presented by horizontal dashed segments.

The structure indicator s_{jk} and the structure parameter S_j are:

$$s_{jk} = |F_{\rm X1} - F_{\rm X2}|/2, \quad \text{and} \quad S_j =< s_{jk} >_j \ . \tag{8}$$

In Fig. 4(a) $F_{\rm X1}$ and $F_{\rm X2}$ are the levels of the crossing points between the window bounds and the segments, connecting 2 neighbor points of MLC in the window edges.

The range indicator r_{jk} and the range parameter R_j are:

$$r_{jk} = (F_{\rm Max} - F_{\rm Min})/2, \quad \text{and} \quad R_j =< r_{jk} >_j \ . \tag{9}$$

In Fig. 4(a) $F_{\rm Max}$ and $F_{\rm Min}$ are the levels of the largest positive and negative peaks of the MLC in the window.

The dimensionless asymmetry indicator a_{jk} and the asymmetry parameter A_j, introduced in the this paper, are:

$$a_{jk} = (F_{\rm Max} - F_{\rm Med})/(F_{\rm Med} - F_{\rm Min}), \quad \text{and} \quad A_j =< a_{jk} >_j \ . \tag{10}$$

Here $F_{\rm Med}$ is the median of the data in the window. In Fig. 4(a) the level of $F_{\rm Med}$ is presented by solid horizontal segment below the level of $F_{\rm AV}$. The value of the asymmetry parameters $A_j > 1$ (and $\log A_j > 0$) and $A_j < 1$ (and $\lg A_j < 0$) indicate positive or negative asymmetry, respectively.

The dependence of the parameters D_j, S_j, R_j and A_j, as well as $H_j = R_j/D_j$ (Sect. 2.4) on the size of the scanning window Θ_j in log–log coordinates are considered as fractal functions. The skewness parameter A'_j (Eqs. 5) is used for comparison with A_j too. These functions are presented In Figs. 5–7 and in the Gallery, together in sub-figures (d,e), like in Fig. 4(b,c).

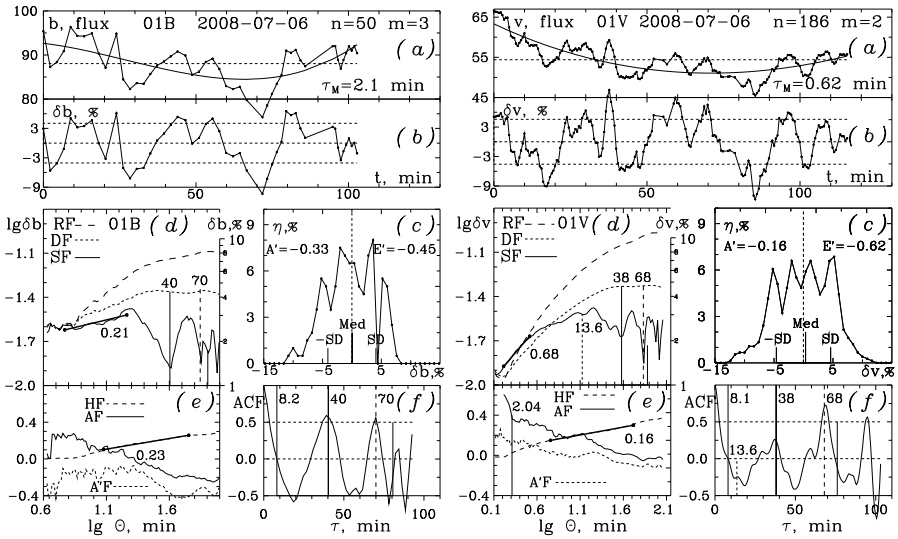

Fig. 5. Analysis of the MLCs #01B (left panels) and #01V (right panels). (**a**): Linearized MLC ($b(t)$ or $v(t)$) (Eqs. 1), with average level (dashed line) and fitting polynomial (solid curve), number of data n and polynomial degree m; (**b**): Relative residual MLC (Eqs. 2), in percents, with the zero level and ± SD levels (dashed lines), with the average time step of the MLC τ_M; (**c**): Histogram of the relative residual MLC (b) with its skewness A' and kurtosis E' (Sect. 1.4). The average, median and ±SD are shown by vertical segments; (**d,e**): Fractal functions RF, DF, SF, AF, HF and A′F (Sect. 2.2–2.5). The right ordinate of (d) is marked out in percents. The thick segments and their labels show the quasi-linear parts of the SF and HF and their gradients. Solid and dashed vertical segments, labeled above, mark primary and secondary quasi-periods, quasi-periods, indicated by the minimums of the SF (Sect. 3.1). An additional short quasi-period of 13.2 min, found only in the V MLC, is marked by short-dashed vertical segment. The thick vertical segment in (e), labeled above, marks the breakdown point of the AF (Sect. 2.5); (**f**): Auto-correlation function (ACF) of the residual MLC (Eqs. 2). The most left vertical segment marks the auto-correlation time $\tau_{\rm ACF}$. Other vertical segments mark the quasi-periods detected by the SF and confirmed by the ACF.

We process the dimensionless relative residual MLCs (Eqs. 2). This approach ensures compatibility of the results, as well as compatibility with other kinds of time series (Fig. 7). Otherwise, if flattened residual MLC (Eqs. 1) is processed, the indicators d, s and r (Eqs. 7–9) must be divided additionally by the average flux in the window $F_{\rm AV}$. Then dimensionless indicators will be usable again.

2.2. Deviation function and its plateau

The deviation function (DF), $\lg D = f(\lg \Theta)$, describes the increasing of the deviation parameter D (Eqs. 7) with the increasing of the window size Θ. In this paper the DFs are presented by short-dashed curves (Figs. 4(b), 5(d)–7(d), Gallery). The DF is used (i) for rescaling of the range function (Sect. 2.4) and (ii) for estimation of the relative energy of the QP

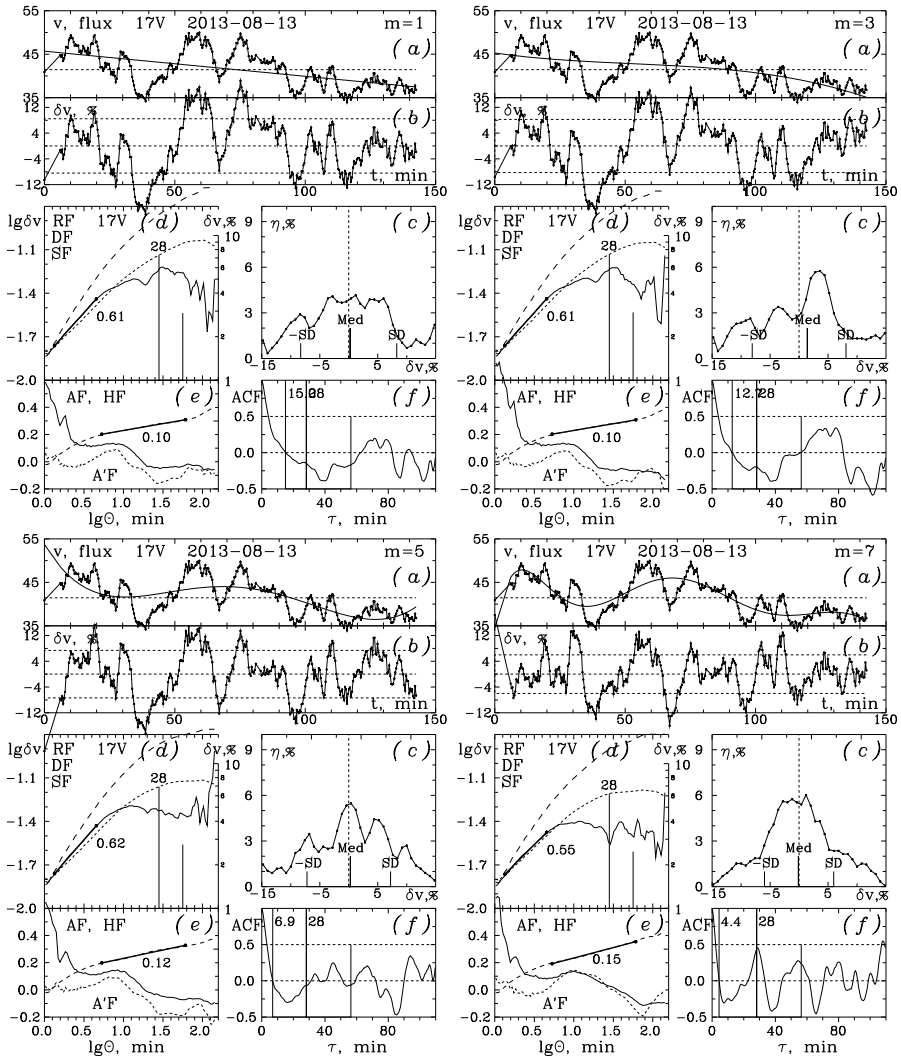

Fig. 6. Effects of the polynomial degree m of the fit on the results from MLC #17V with number of points $n = 142$ and time step of the MLC $\tau_M = 0.4$ min. The polynomial degrees m are 1, 3, 5 and 7. The standard deviations are 3.5, 3.4, 3.0 and 2.5, respectively. The histogram changes significantly. The structure gradient stays almost unchanged. The Hurst gradient increases weakly. The auto-correlation time decreases 3.4 times and the quasi-periods, detected by the structure function and the ACF, tend to coincide. The polynomial fit of 7-th degree is adopted as optimal. See Fig. 5 for details.

flux variations and the correlation between the QP value and this energy (Sect. 3.3).

The DF of the MLC poses a simple universal behavior. While Θ is small

and increases, DF incorporates larger MLC structures, i.e. larger variations. When the window, growing up, begins to include a QP structure, the quantity of new larger deviations decreases and the DF tends to a plateau. The plateau level of the DF characterizes the energy of the variations, associated with the main (dominating) QP structure, together with the energy of its substructures.

The DFs of the sunspot index and planetarium visits follow the same behavior. However, while the heights of the MLCs plateau levels are about 5%, the heights of the plateau levels of the sunspot index and planetarium visits are about 90% and 75% (Fig. 7(d)).

In Fig. 4(b) the level D(1) corresponds to the QP P(1), found by the position of the local minimum of the SF (Sect. 2.2, 3.2). In Figs. 5(d)–7(d) and in the Gallery the quasi-periods are labeled just above their levels in the DFs.

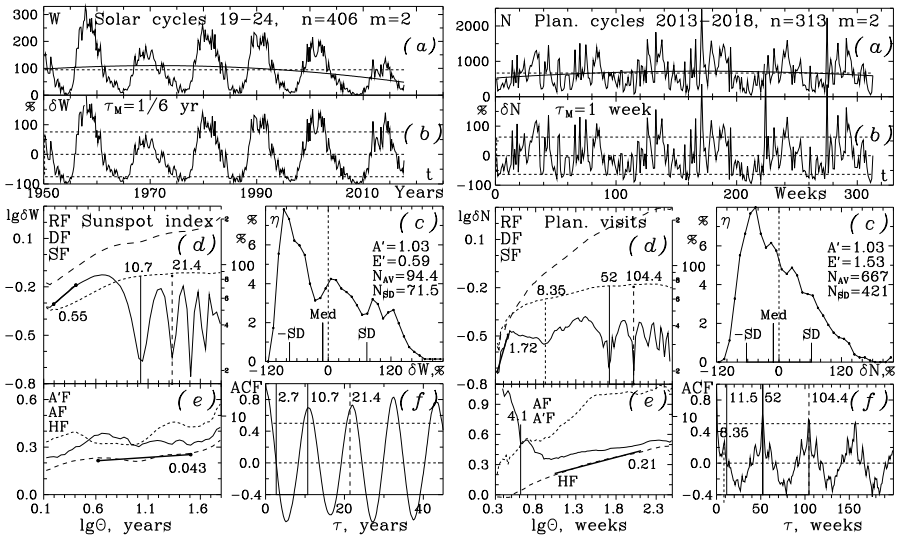

Fig. 7. Application of the used methodics on the behavior of the sunspot index W in the last 6 cycles (left panels) and the number of the visits of the Smolyan planetarium N in the last 6 years (right panel). (**a,b**): Original and flatten time series, like linearized and flattened MLCs; (**c**): Histograms of the flatten time series; (**d,e**): Fractal functions; (**f**): Aut-correlation fuction. See Fig.5 for comparison.

2.3. Structure function and structure gradient

The structure function (SF), $\lg S = f(\lg \Theta)$, describes the change of the structure parameter S (Eqs. 8) with the increasing of the window size Θ. In this paper the SFs are presented by solid curves (Figs. 4(b), 5(d)–7(d), Gallery). The SF is used in two ways: (i) the gradient of the initial part

of the SF is used to characterize the dominating process which drives the variability – local shots or global disk instabilities and (ii) the local minima of the SF are used as detectors of QPs.

While Θ is small and increases, the SF increases almost linearly. The relevant slope coefficient, known as **structure gradient** (SG), is:

$$SG = \Delta \lg SF(\Theta)/\Delta \lg \Theta \tag{11}$$

The quasi-linear part of the SF is presented in Figs. 5(d)–7(d) and in the Gallery by thick segment, labeled with the SG value.

The SG value depends on the feedback of the flux variability and it is an important characteristic of the apparent chaos of the MLCs (Di Clemente et al., 1996, Kawaguchi et al.,1998). A value $SG > 0.5$ indicates a variability, driven mainly by shots (impulses). A value $SG < 0.5$ gives privilege to global flux instabilities of the disk. The last mentioned case was suspected for KR Aur (Bachev et al., 2010). Examples follow.

In Fig. 5(d), left panel, for the MLC #01B with average time step $\tau_{\rm M} = 2.1$ min and poor defined initial part of the SF, we derive $SG = 0.22$. In contrast, in Fig. 5(d), right panel, for the MLC #01V, with $\tau_{\rm M} = 0.62$ min and well defined initial part of the SF, we derive $SG = 0.68$. The SG depends significantly on the time resolution of the MLC. Figure 6 shows that the SG depends weakly on the polynomial degree, taking values between 0.55 and 0.62.

A comparison with sunspot index and planetarium visits is again useful. In Fig. 7, left panels, the well pronounced 10.7 yr large scale sunspot cycle plus the faint short time variations, produce moderate SG value, $SG = 0.55$. In Fig. 7, right panels, the badly pronounced 1 yr cycle of the planetarium visits plus the dominating strong short time impulses, produce extremely high SG, $SG = 1.72$. From this point of view the behavior of the flux variation of RS Oph seems formally close to the behavior of the short scale variation of the sunspot index.

Figure 8(a) shows the distributions of the SGs of 58 MLCs. They take a range from 0.1 to 0.9, with a peak at 0.48 ± 0.16. This value is an evidence that the flux variations in time scale from 15 to 60 min may be due to both local obscures/shots and global instabilities with alternate superiority.

We note that due to the low time resolution in many MLCs, mainly in B band, the SGs are poorly pronounced and they seem to be underestimated. However, Fig. 9(a) does not show significant correlation between the time step $\tau_{\rm M}$ and SG of the MLC. According to Fig.9(b) the SG does not correlate also with the auto-correlation time $\tau_{\rm ACF}$. Therefore, in our cases the SG seems to be robust, but hardly derived parameter.

The SF is introduced originally for studying of long light curves in the form $\phi(\Theta) =< [F(t) - F(t+\Theta)]^2 >$ (Hughes, Aller & Aller 1992). Here Θ is the time interval between two measurements and the broken brackets express average over all measurements with the same time interval. Such SF is utilized successfully for light curves of 10 LBV stars by Gantchev et al. (2017). Practically, this kind of SF is based on the indicator $\phi_{jk} = s^2_{jk}$ (Eqs. 6). However, following Di Clemente et al. (1996) we use the SF $\phi^{1/2}_{jk}$ instead ϕ_{jk}, which is applied for studying of light curves of AGNs. Such SF

may be compared directly with the relevant DF and RF(Figs. 5(d)–7(d), Gallery).

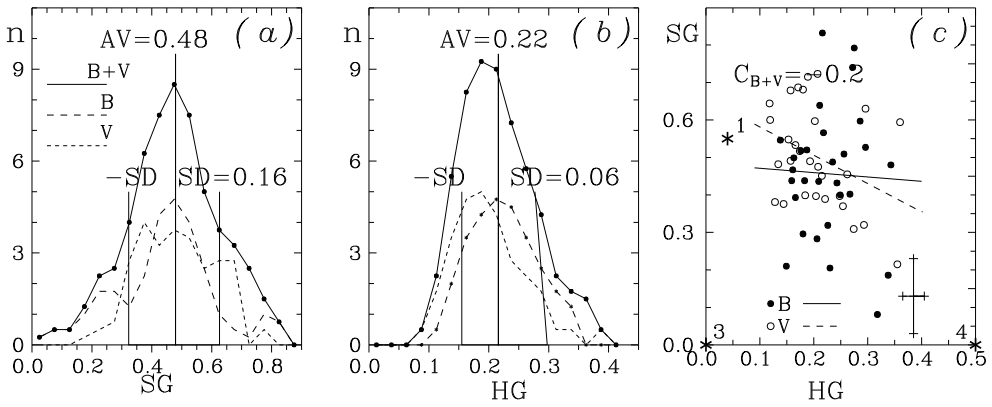

Fig. 8. (**a,b**): Distributions of the structure gradient (SG, Sect. 2.3) and Hurst gradient (HG, Sect. 2.4) for 58 MLCs. Dashed or solid segments show the separate (B or V) distributions or the common (B plus V) distribution. (**c**): Mutual distribution of both gradients. Solid and dashed lines present the ordinary regressions for B and V data, respectively. The asterisks show the positions of the time series of sunspot index (1), uniform random process (3) and normal random process (4). The planetarium visits with $SG = 2.72$ and $HG = -0.21$ take place far above the top of this diagram.

2.4. Range function, Hurst function, Hurst gradient and fractal dimension

The range function (RF), $\lg R = f(\lg \Theta)$, describes the increasing of the range parameter R (Eqs. 9) with the increasing of the window size Θ. In contrast to the DF and SF, the RF does not reach saturation. The RF is constant for uniform random processes only. In this paper the RF is presented by dashed curve (Figs. 4(b), 5(d)–7(d), Gallery).

The RF is used together with the DF in a rescaled RF, called also Hurst function (HF), $\lg(R/D) = f(\lg \Theta)$. The initial part of the RF is derived from short window sizes Θ, which contains just a few large deviations. By this reason the RF and HF are initially underestimated. However, at larger Θ the HF grows up more slow and tends to a straight line with so called **Hurst gradient**(HG):

$$HG = \Delta \lg HF(\Theta)/\Delta \lg(\Theta). \tag{12}$$

The quasi-linear parts of the HFs are presented in the sub-figures (e) by thick segments, labeled with their HGs. The HG is used (i) to characterize the auto-correlation in the MLC and (ii) to estimate the fractal dimension of the MLC (Eq. 13).

The HF and HG, based on the dull the peak-to-peak amplitude, are introduced historically by Harold Hurst (1951). He asked whether fluctuations in the cumulative discharge of the Nile River scale similarly. Note that our HFs and our HGs are based on the half of the peak-to-peak amplitude (Eq. 9, Eq. 12) and our HG is less of the original Hurst value by 0.3.

Mandelbrot & Wallis (1996) explain this behavior in terms of scale-invariant long-term correlations and introduce fractal modeling of time series. They emphasize also that in noncyclic statistical processes the HG possesses a significant robustness in the estimation of the auto-correlation in the MLCs, as follows.

A value of HG in the range 0–0.5 indicates a time series with short-term positive autocorrelation, i.e. with short-term switching between high and low values in adjacent data points. A value of HG in the range 0.5–1 indicates a time series with long-term positive autocorrelation. From this point of view, values of HG about 0.5 are not useful. Hurst (1951) derived $HG = 0.77$ for the Nile River. (The relevant our value id 0.47.) The interpretation is: every significant positive flow peak has long time tail because it is due to the contribution of a large feeder of the Nile. Analogous phenomena in our MLCs are missing, at least on time intervals < 60 min.

Despite of some semi-cyclic character of some MLCs, we can not bypass the HG as robust characterizer of apparent chaos of time series and robust estimator of the fractal dimension. In contrast to the SG, the HG of our MLCs is defined by well pronounced quasi-linear parts of the HFs. Because of the definitions (Eq. 9, Wq. 12) the value of the HG is related with the **fractal dimension** (FD) for 1D random process:

$$FD = 2 - HG - 0.3. \tag{13}$$

Figure 8(b) shows the distribution of our HG (Eq. 12) for 58 MLCs. The range is 0.1–0.4 with average $0.22(\pm 0.06$. This HG value fors not give evidence about domination of short-time auto-correlations. The relevant average FD for our 58 MLCs is $FD = 1.48 \pm 0.06$.

Comparison with "edge" time series is again useful. In the case of a uniform random process, the DF and RF tend to a constant and the expected value is $HG = 0$. The central limit theorem in the statistics involves a power law for the sum of N independently distributed and bound random variables of mean 0. The size of the sum scales as $N^{1/2}$. Therefore, for a random process with normal distribution of the deviations, the expected HF is $\lg R/D \to 0.5 \times \lg \Theta$. So, our $HG \to 0.2$, giving $FD \to 1.5$.

The variations of the sunspot index are characterized by our $HG = 0.043$. This value gives evidence for short-time autocorrelation, due to the domination of weak short shots, in spite of the presence of well pronounced large scale periodicity (Fig. 7, left panels). The respective FD is 1.66. But, while the process is obviously periodic, this is not an ultimate estimation.

In the variations of the planetarium visits we derive our $HG = 0.21$. This value shows privilege for short-time autocorrelation, due to the domination of strong short shots, in presence of weak pronounced large scale periodicity (Fig. 7, right panels). The respective FD is 1.49. The typical HG values in this work give evidence that the MLC structure is close to the structure of the planetarium visits.

Figure 8(c) juxtaposes SGs and HGs. They do not correlate and do not hint to some classification of the MLCs (at leat here). The points of the SGs and HGs of the MLCs seem somewhat bound from the comparative 4 "edge" time series.

Figure 9(c) show that our HG correlates with the time step $\tau_{\rm M}$. Note that in Fig. 5(d), left panel, under low time resolution ($\tau_{\rm M}$ = 2.1 min), we found $HG = 0.23$. But in Fig. 5(d), right panel, under high time resolution ($\tau_{\rm M}$ = 0.62 min), we found $HG = 0.16$. The increased HG in case of high time step (low time resolution) of the MLC is due to the observational transform (smearing) of strong short-time shots (peaks) into more weak long-time shots. Then the short-term autocorrelation in the MLC is suppressed and the HG becomes overestimated. This is the reason of the correlation between τ_M and HG in Fig.9(c). By this reason any rescaling of the MLC for "increasing" of its resolution causes overestimation of the HG.

Nevertheless, the regression intercept in Fig. 9(c), $HG_0 = 0.16 \pm 0.05$ (for B plus V data together) gives another, a little bit higher estimation of the mean FD of the MLCs, FD=1.68 ± 0.05.

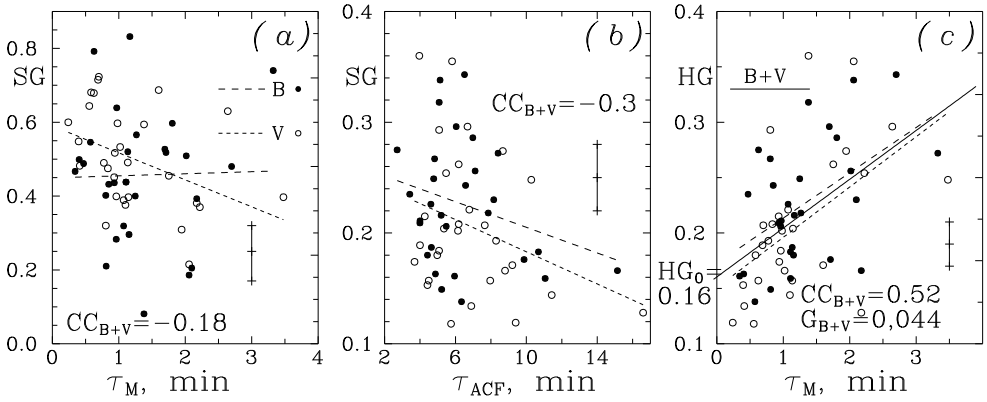

Fig. 9. (**a,b**): Juxtaposition of SG or HG with time step $\tau_{\rm M}$ and autocorrelation time $\tau_{\rm ACF}$ of the MLCs. The ordinary regressions for B, V and B plus V data are presented by dashed, short-dashed and solid lines, respectively. The correlation coefficients concerns B plus V data together; (**c**): Juxtaposition of SG and HG and estimation of $HG_{\rm AV}$ and HG_0 for $\tau_{\rm M}$=0, shown along the ordinate axis. Vertical bars correspond to the typical individual errors.

2.5. Asymmetry function and the shortest shots in the MLC

The skewness indicator a' and skewness parameter A' (Eqs. 5) lead to the skewness function (A′F), $A'F = f(\lg \Theta)$. This function (without logarithm) is shown by dashed curves in Figs. 5(e)–7(e) and in the Gallery. Typical

large scale behavior of the A′F is a decrease. The average final values are about 0.1±0.3, as in Fig. 3(a).

In the present paper we introduce another asymmetry indicator and parameter, a and A (Eqs. 10). The relevant asymmetry function (AF), is $\lg A = f(\lg \Theta)$. This function (with logarithm) is presented by solid curve in Figs. 5(e)–7(e) and in the Gallery. The general behavior of $\lg A$ is similar to the behavior of A', but the AF is preferable instead A′F for two reasons.

The first reason is that the AF reveals clearly a strong asymmetry of the flux changes at the short time scale, in windows containing 3–5 adjacent MLC points. In such windows the flux often grows up with increasing rate and grows down with decreasing rate. Fig. 4(d) shows typical fragments of MLCs with 5 and 4 adjacent points, where the asymmetry indicator a takes large values.

Figures 10(a,b) show parts of real MLCs where 3 adjacent points give very high values of a. Figures 10(c,d) show the relevant very high initial parts of the AFs. This means that faint shots with short durations have wide presence in the MLCs.

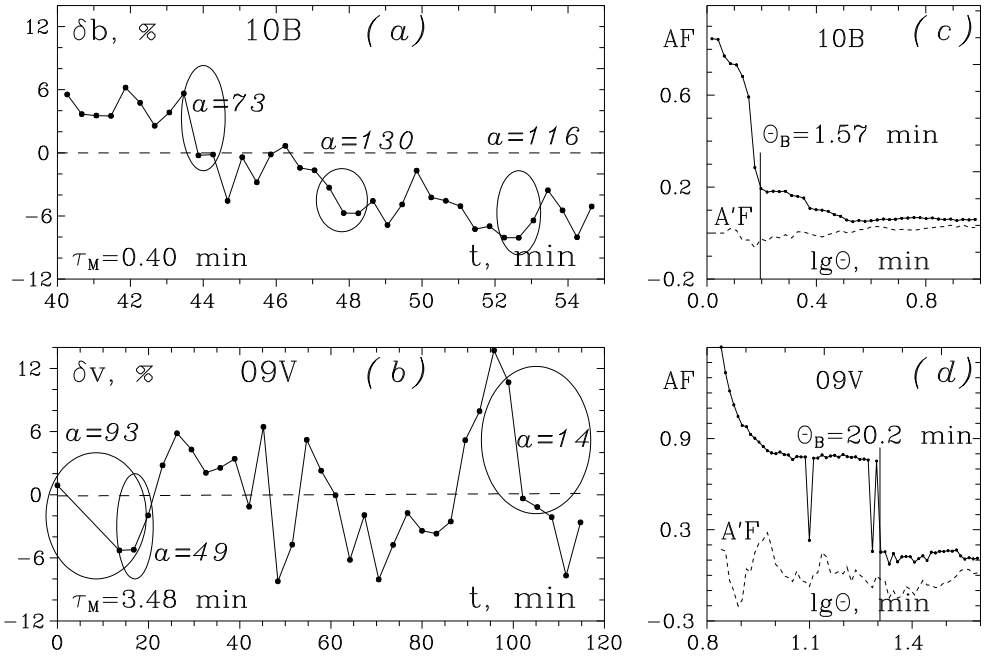

Fig. 10. (**a,b**): Part of the MLC #10B (71 points) with the shortest time step (0.4 min) and the entire MLC #09V (34 points) with the largest time step (3.5 min). The ellipses encompass triades of points giving very high asymmetry indicators a; (**c,d**): The relevant asymmetry functions showing very high values at short time scales and well pronounced breakdown time-points, $\Theta_{\rm B}$ at 1.57 min and 20.2 min, respectively.

The second reason is that in contrast to A′F, in the majority of the MLCs (48 cases), the AF shows well defined **breakdown time-point** (BT), $\Theta_{\rm BT}$. The BT is marked by thick vertical segment in Figs. 4(c), 5(e)–7(e) and in the Gallery. Though, B MLCs ## 1, 12, 16, 17 ,20 and 21 and V MLCs ## 2, 13, 16 and 17 do not pose BTs.

Figure 11 illustrates the usefulness of AF instead A′F – the remarkable dependence of the BT $\Theta_{\rm B}$ on the time step $\tau_{\rm M}$. This dependence has an exponential shape, i.e. linear shape under logarithmic ordinate. The intercept ought to be interpreted as the half-time, $\tau_0/2$, of the shortest shots in the MLC variations. So, the mean duration of the elementary shot is roughly estimated to be $\tau_0 = 3.61 \pm 0.79$ min.

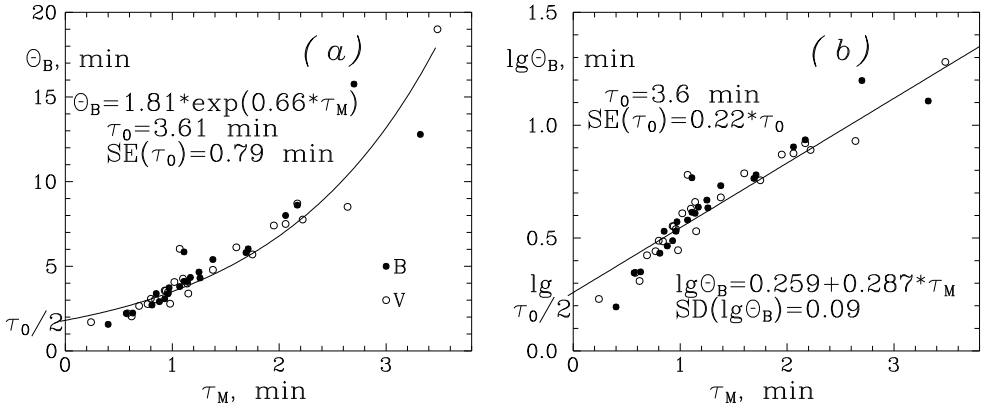

Fig. 11. Dependence of the BT $\Theta_{\rm B}$ of the AF on the time step $\tau_{\rm M}$ presented by an exponent (a) and a power function (b). "SE" means standard error. The regression intersepts are interpreted as characteristic time duration of the shortest shots.

For comparison, in Fig. 7(e) the AFs and A′Fs of the sunspot index W and the planetarium visits N show a global increase. The AFs tends to $A \approx 2$ and $A \approx 3$, respectively. In contrast to the initial part of the AF for W, the initial part of AF for N has high values, just like the majority MLCs, with BT about $\tau_0/2 = 4$ weeks. The reason is a presence of about 8 weeks inter-year QP, corresponding to the scholar schedule (already marked in Fig. 7(d), right panel). The variations of W do not show such particularity. The reason is obviously the low resolution of the used time series, $\tau_{\rm M} = 2$ months, while the most of the sunspot groups last for only a few days.

3. Distributions of the quasi-periods

In Paper I, working in magnitude scales, we show that QPs exists in all MLCs. In the present paper, working in linearized and flattened MLCs (Eqs. 1 and 2) we justify the QPs and their distribution.

3.1. Structure function, quasi-periods and auto-correlation function

The SF (Sect. 2.3) is also a good detector of QPs in the apparent chaos of the MLC. After the initial quasi-linear part of the SF, while the data window Θ continues to increase, the SF tends to saturate like the DF (Sect. 2.2), but typically slower and at lower level. However, when the window size Θ begins to envelope a repeating structure, the SF tends to a local minimum. From this point of view in a periodic time series the SF plays just the role of the the phase dispersion minimization function (Lafler & Kinman, 1965). A very good demonstration on a Cepheid light curve is shown by Ganchev et al. (2017, Fig. 5).

The position of a local minimum of the saturated part of the SF is estimation of a QP in the MLC. In Figs. 4(b), 5(d)–7(d) and the Gallery, such QPs are marked by vertical segments. If the MLC is long enough , it may contain repeat(s) of a dominate structure with some QP, P. Then the SF shows "harmonic" minima also at Θ=2P, Θ=3P, etc. The shortest well unveiled QP with value P is considered as main, or primary, or basic. In the diagrams it is marked by solid vertical segment, labeled above by the value of P. The relevant harmonic period 2P, if it is enveloped by the SF, is marked by a shorter solid vertical segment without label (Figs. 5(d)–7(d), Gallery). Main QPs are found in all 58 MLCs (Tables 3 and 4).

Accounting to the local minima of the SF, we unveiled 20 other remarkable QPs, not harmonic (not multiple) of the main QPs (Table 5). Any such QP is considered here as alternative, or secondary, or additional. Such QP is marked by dashed vertical segment, labeled above by the relevant P. The "harmonics" of the alternative QP, with value 2P, if it is enveloped by the SF, is marked by shorter dashed vertical segments, without label. For example, in Fig. 5(d) the values of the primary QPs in B and V MLCs are 40 min and 38 min, respectively. The secondary QPs are 70 and 68 min, respectively.

In 6 of our MLCs (## 07B, 08B, 10B, 07V, 16V and 21V; Table 5) we find also "tertiary" QPs, which are not multiple of the primary or the secondary QPs. They are marked by short-dashed vertical segments.

Sometimes a faint local minimum of the SF hints of a QP with $P < 15$ min. We revealed such short QPs in 13 MLCs, 9 in B and 4 in V band (Table 5). All these QPs are marked by short-dashed vertical segments, labeled from above. For example, such QP with $P = 13.2$ min, is detected in Fig. 5(d), in the V MLC.

In this paper all QPs, detected by SFs, are checked and confirmed by relevant ACFs of the MLC. The ACF has the form $f(\tau) =< F(t)F(t + \tau) >$ and it is utilized on uniformly sampled and flattened time series. Here τ is the time lag of the measures. The QPs cause local maxima in the ACF (Fig. 5(f)–7(f), Gallery), marked in the same manner as in the diagrams of the SFs. The most left vertical segment in sub-figures (f) marks the characteristic auto-correlation time $\tau_{\rm ACF}$ – the time in which the ACF crosses the zero level at first time.

Some MLCs have short time interruptions for justifications of the telescope positions. Such MLCs are unfit for ACF analysis. They are additionally re-sampled with steps equal to the average time step τ_M of the MLC.

The re-sampled MLCs are used only for the ACFs. Re-sampling with increasing of the resolution increases artificially the HG, as it is shown in Fig. 6.

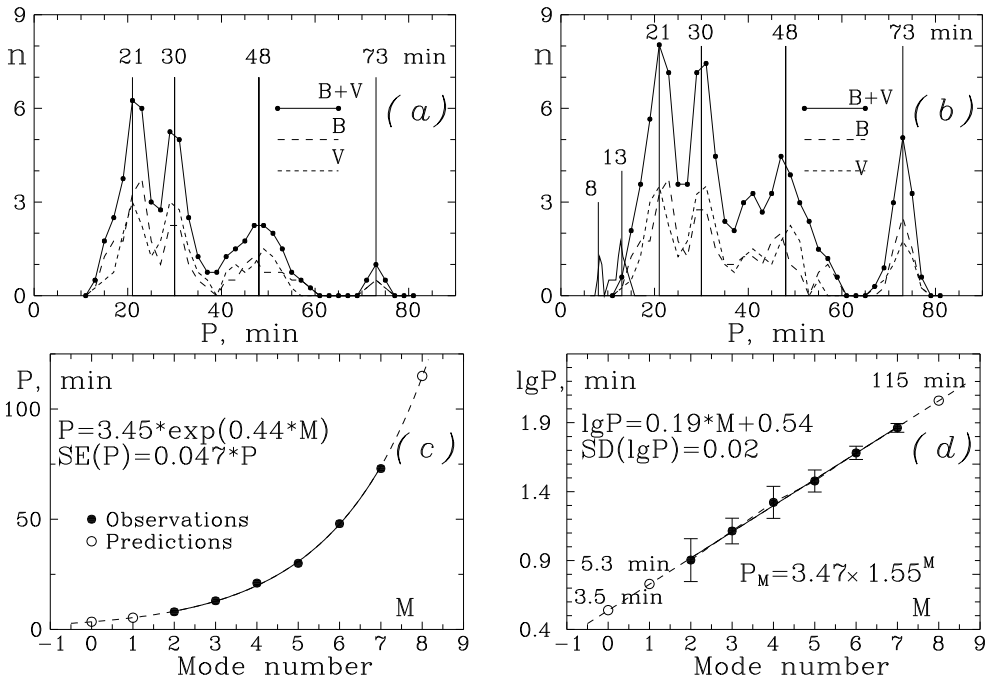

Fig. 12. Distributions of 97 QPs from 58 MLCs of RS Oph in 6 modes. (**a,b**): Histograms of the QPs separately (dashed curves) and commonly (solid curves) – only the primary 58 QPs (a) and all 97 QPs (b); (**c,d**): Increase of $\lg P$ with the serial number of the QP mode M for 6 observed mode values with a relative error about 5% of P – as exponent (c) and as power function (d).

An unexpected QP of 8.35 weeks (2 months) is found in the planetarium visits (Fig. 7(d), right panel). The reason is the specific annual regime of the Bulgarian pupils and students.

3.2. Modes in the distribution of the quasi-periods

In this paper 97 QPs are detected by DFs and confirmed by ACFs. Among them 58 are primary, 20 are secondary, 10 are tertiary and 13 are found additionally as quite short (sub-figures (d) and (f) in Fig. 5 and Gallery). The analyzed MLCs are really very complicated.

Figure 12(a) presents the distribution of the primary 58 QPs only, 29 in B MLCs and 29 in V MLCs. They follow 4 well pronounced modes, at 21, 30, 48 and 73 min. Figure 12(b) shows this distribution after including

of 20 secondary, 6 tertiary and 13 short QPs. The same 4 modes are well revealed and the shortest 13 QPs contribute 2 QP modes – at about 8 min and at about 13 min.

Figure 12(c,d) presents the basic result in this paper – 6 observed mode times of the QPs, which follow well an exponential function on the serial number M:

$$P_M = 3.45 \times \exp(0.44 \times M) \quad \text{or} \quad \lg P_M = 0.54 + 0.19 \times M. \tag{14}$$

The respective power dependence of the quasi-period P as function on the serial number of the mode M is:

$$P_M = 3.48 \times 1.55^M, \tag{15}$$

with standard error of 4.7%.

These dependences seem to be forms of a resonance consequence with quotient $1.55 \approx 3/2$. They predict at least 3 other modes, at 3.5 min, 5.3 min and 115 min, but these modes are undetected in this work.

Figure 13 presents the QP modes over the logarithmic time scale where they are placed along an arithmetic sequence. Note that the shortest shots, with durations about 3.6 min (Sect. 2.5), take position close to mode $M = 0$. The quotient of the power function is invariant toward the zero-point of the serial numbers. By this reason we assign $M = 0$ to the shortest suspected QP, i.e. $P(0) = 3.5$ min.

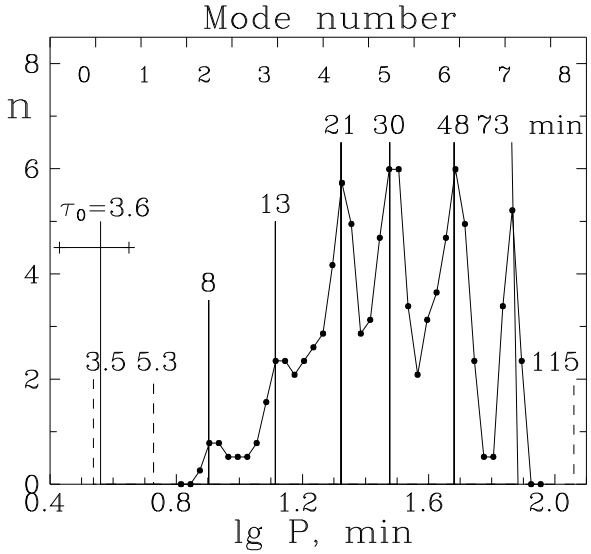

Fig. 13. Distribution of 97 quasi-periods of RS Oph over logarithmic time scale in 6 observed modes, marked by solid vertical segments. Other 3 predicted modes are marked by dashed vertical segments. The shortest shots, with duration 3.6 ± 0.8 min (Sect.2.5), marked too, are close to the predicted short with $P = 3.5$ min.

Figure 14(a) unveils the detectability of the QPs in juxtapositions with the monitoring time $T_{\rm M}$. While the left-up half of the diagram is empty, the detection zone is well bounded by the bisektrise of the coordinate axes. The number of the large QPs ($P > 60$ min) is small, because they are detectable only in the very long MLCs. Numerous QPs with $P = 20-40$ min are found because they are detectable in almost all MLCs. The right-down corner of the diagram is almost empty because various short time structures with $P < 15$ min are smeared or their QP evolve in a long MLC. We found only 13 such QPs (Sect. 3.1), included in the down part of the diagram.

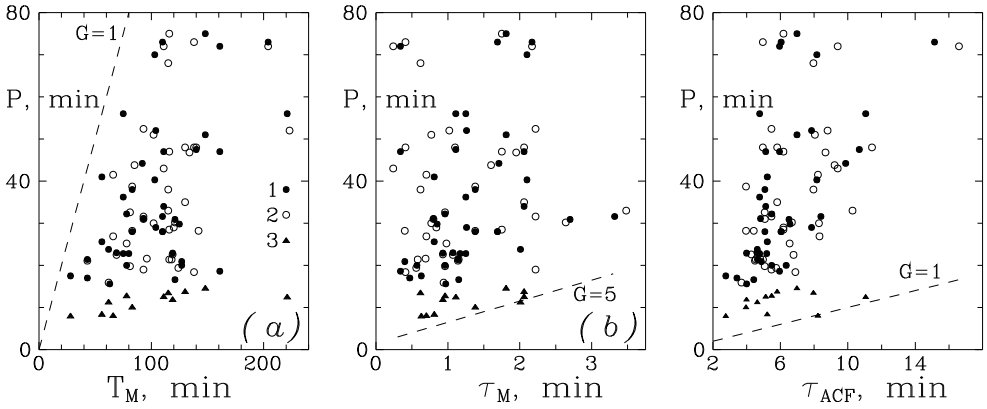

Fig. 14. Detectability of the 97 QPs – 42 in B MLCs (1), 42 in in V MLCs (2), and 13 the shortest, commonly in B and V (3), in juxtaposition with the MLC observing time $T_{\rm M}$ (**a**), the MLC time-step $\tau_{\rm M}$ (**b**) and the ACF time $\tau_{\rm ACF}$ (**c**).

Figure 14(b,c) juxtaposes the QP Ps with the MLC time step $\tau_{\rm M}$ and ACF time $\tau_{\rm ACF}$. The detection zones are bound from the right-bottom by lines with gradients about 5 and about 1, respectively. The shorter QPs may be detected with shorter time-step. Otherwise, here the hidden short time structures cause increasing of the ACF time. Obviously, the applied QP detection is the most effective for time structures with sizes 20–60 min.

Two main conclusions are obvious here. First, the modes of the QPs follow well exponential (or power) dependence, similar to a 3/2 resonance sequence. Second, the well defined bounds of the detection zones in Fig. 14 give evidences for the uniformity and the efficiency of the method, used for unveiling of QPs.

3.3. Quasi-periods and their flickering energies

In the end the correlation between the QPs and their "energy", revealed in Paper I, will be revisted and justified. The plateau levels of the DF δb or δv (Sect. 2.2), corresponding to the QPs P, detected by the SF (Sect. 3.1) are a measure of the relative energy of the flickering, associated with the QP structure and its cumulative substructures.

Figure 15(a,b) shows the histograms of the energies and their correlations with the QP. The QPs in the MLFs #05V, #20V1 and #20V2 correspond to abnormal high energies. They are shown in Fig. 15(b), but not used in the calculations.

Figure 15(a) shows that the energies δb or δv belong to the interval 0.02–0.08 (approximately from 0.02 to0.08 mag). The B distribution is unimodal, with peak at 0.046 ± 0.008, with clear positive asymmetry. However, the V distribution is somewhat flat, with low peak at 0.051 ± 0.012. The apparent flatness is due to the heavy right wing of this distribution.

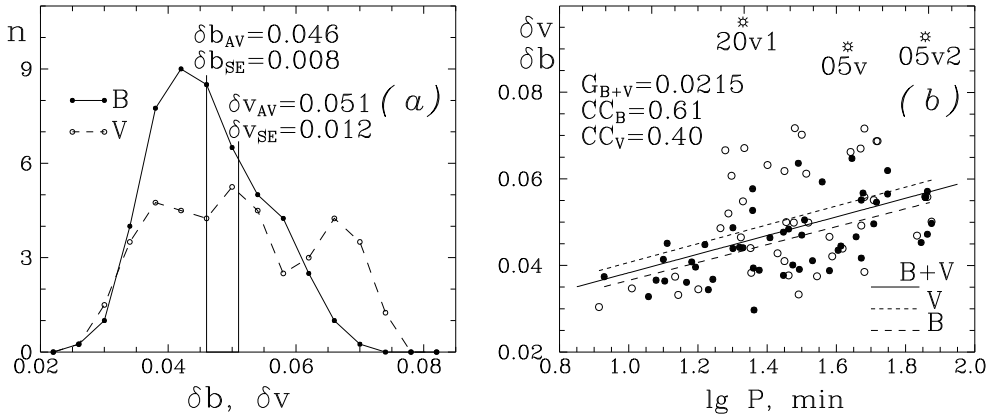

Fig. 15. The QPs and their flickering energies δb or δv for 93 QPs. (**a**): Histograms and average values of the energies; (**b**): Regressions of the energies (separate and common) in respect to lg P. The QPs with the most deviated energies (asterisks) are not used in calculations.

Figure 15(b) shows that the flickering energies correlate with the logarithms of the QPs with CCs 0.61 and 0.40 (in Paper I – 0.68 amd 0.47), in B and V bands, respectively. The regression gradients are about 0.02 (In Paper I – 0.04 and 0.03 in B and V, respectively).

Figure 15 gives evidence that the relative energy of the flickering correlates, at least weekly, with the QPs. The distinctions between this Fig. 15 and Fig. 10 in Paper I are small and they are due to the use of different scales of the MLCs.

4. Conclusions

In this paper a system of specific statistical methods (fractal approach) is applied to the MLCs of the flickering source in the RS Oph. The main results are, as follows.

1. The more bright MLCs of the flickering source are more red (Fig. 1(a,b,c), cf. Zamanov et al. 2018). Rare strong single shots in the MLCs of the flickering source appear also more red than the neighbor parts of the MLC.

2. The distributions of the skewness and kurtosis of the deviations of the MLCs show that in about 1/4 of the cases the flickering is similar to a normal random process. Otherwise, in about 1/2 of the cases the flickering is similar to an uniform random process. Then the light curves of the flickering source pose deficit of short deviations (Fig. 2(b), Fig. 3(a,b)). Deficit of large deviations, such as negative impulses (obscures) or positive impulses (shots) is obvious too (Fig. 3(a,b)). In such cases the flickering fluctuations seem similar to oscillations. Various light curves are available. They may show quasi-periods, like the variations of the sunspot index or they may show sharp variations like the changes of the planetarium visits.

3. The distributions of the gradients of the structure function and Hurst function (Fig. 8(a,b)), show that the light curves are significantly different from the uniform and normal random processes. Simultaneously, the flickering is similar to the sunspot index variations by its structure gradient, i.e. by presence of faint short shots and more strong long quasi-periods. The flickering is similar also to the planetarium visit variation.It gives fractal dimension 1.48 ± 0.06, corresponds to indeterminate autocorrelation. The relevant fractal dimensions for the the sunspot index and planetarium visits are 1.66 and 1.49, respectively (Part 2.4).

4. Generally, local disk shots and global disk instabilities are present in the intra-night flickering with changeable superiority, with some privilege of the disk instabilities. The mutual distribution of structure gradients and Hurst gradients in Fig.8(c) take large place between the comparative 4 "edge" time series, but does not lead to some classification of the light curves.

5. The asymmetry function, introduced in this paper (Sect. 2.5), gives estimation of the mean duration of the shortest positive shots, 3.6 ± 0.8 min (Fig. 11).

6. Quasi-periods are found in all flickering time series. The quasi-period of about 21 min corresponds the most widespread time structure size. The modes in the distribution of the quasi-periods are placed at about 8, 13, 21, 30, 48 and 73 min (Fig. 12, 13). The respective power dependence of the quasi-period P as function on the number of the mode M is $P_M = 3.48 \times 1.55^M$, with standard error of 4.7%. This function predicts modes also at 3,5, 5.3 and 115 min, which are not detected in this work. However, the characteristic duration of the elementary shot, 3.6 ± 0.8 min (Fig. 11), corresponds well to the predicted mode at 3.5 min. The mode distribution corresponds also to a power function with base $1.55 \approx 3/2$, hinting about somewhat 3/2 resonance.

7. The weak correlations between the quasi-period and its cumulative flickering energy (plateau level of the density function), found in Paper I, is confirmed with the slope coefficient 0.02 (Fig. 15).

Acknowledgments: This work is supported by the grant КП-06-H28/2 08.12.2018 (Bulgarian National Science Fund). The authors thank to the staff of the Smolyan Planetarium and especially to Mrs. Hristina Kalaydzhieva for the data about the planetarium visits.

The authors are especially grateful to the anonymous referee for its attention to this paper and for the numerous recommendations.

References

Bachev, R., Boeva, S., Georgiev, T., et al. 2011, Bulgarian Astronomical Journal, 16, 31
Bessel, M. S. 1979, PASP, 91, 589
Brandi, E., Quiroga, C., Mikołajewska, J., Ferrer, O. E., & García, L. G. 2009, A&A, 497, 815
di Clemente, A., Giallongo, E., Natali, G., Trevese, D., & Vagnetti, F. 1996, ApJ, 463, 466
Evans, A., Bode, M. F., O'Brien, T. J., & Darnley, M. J. 2008, RS Ophiuchi (2006) and the Recurrent Nova Phenomenon, ASP Conf. 401
Falconer, K., 1997, Techniques in Fractal Geometry, John Willey & Sons, Chichester
Fekel, F. C., Joyce, R. R., Hinkle, K. H., & Skrutskie, M. F. 2000, AJ, 119, 1375
Gantchev, G., Valcheva, A., Nedialkov, P., & Ovcharov, E. 2017, Bulgarian Astronomical Journal, 26, 16
Georgiev, T., Antov, A., Bachev, R., et al. 2012, Bulgarian Astronomical Journal, 18, 36
Georgiev, T., Zamanov, R., Boeva, S., et al. 2019, Bulgarian Astronomical Journal, 30, 83-98. Paper I
Hastings H. M., Sugihara G., 1995, Fractals. A user guide for Natural Sciences. Part IV-9. Oxford University Press.
Hughes, P. A., Aller, H. D., $ Aller M F 1992 ApJ 396 469
Hurst, H.E. (1951) Transactions of American Society of Civil Engineers. 116: 770.
Joanes, D. N.; Gill, C. A. (1998). "Comparing measures of sample skewness and kurtosis". Journal of the Royal Statistical Society, Series D. 47 (1): 183189.
Kawaguchi, T., Mineshige, S., Umemura, M., Turner, E. L., 1998, ApJ 504, 671
Kundra, E., & Hric, L. 2014, Contributions of the Astronomical Observatory Skalnate Pleso, 43, 459
Kundra, E., Hric, L., & Gális, R. 2010, Binaries - Key to Comprehension of the Universe, 435, 341
Lafler, J., & Kinman, T.D., 1965, ApJS 11, 216
Mandelbrot, B.B., 1982, The fractal Geometry of Nature, Freeman, New York
Mandelbrot, B. B.; Wallis, J. R. (1968). "Noah, Joseph, and operational hydrology". Water Resour. Res. 4: 909918.
Mandelbrot, Benoit B.; Wallis, James R. (1969-10-01). "Robustness of the rescaled range R/S in the measurement of noncyclic long run statistical dependence". Water Resources Research. 5 (5): 967988.
Mikołajewska, J., & Shara, M. M. 2017, ApJ, 847, 99
Narumi, H., Hirosawa, K., Kanai, K., et al. 2006, IAU Circ., 8671, 2
Russ, J.C., 1994, Fractal Surfaces, Plenum Press, New York & London
Shenavrin, V. I., Taranova, O. G., & Nadzhip, A. E. 2011, Astronomy Reports, 55, 31
Walker, A. R. 1977, MNRAS, 179, 587
Wynn, G. 2008, RS Ophiuchi (2006) and the Recurrent Nova Phenomenon, ASP Conf. 401, 73
Zamanov, R., Latev, G., Boeva, S., et al. 2015, MNRAS, 450, 3958
Zamanov, R. K., Boeva, S., Latev, G. Y., et al. 2018, MNRAS, 480, 1363
Zombeck, M.V., 1990, Handbook of space astronomy & astrophysics, Second edition, Cambridge University Press